Selecting and Testing of Cement-Bonded Magnetite and Chalcopyrite as Oxygen Carrier for Chemical-Looping Combustion

energies

MDPI

Article

Selecting and Testing of Cement-Bonded Magnetite and Chalcopyrite as Oxygen Carrier for Chemical-Looping Combustion

Mengjun Li [1], Teng Zheng [1], Daofeng Mei [1,2,*], Baowen Wang [3] and Jingjing Ma [4]

[1] College of Engineering, Huazhong Agricultural University, Wuhan 430070, China; mengjun.li@webmail.hzau.edu.cn (M.L.); teng.zheng@wellintech.com (T.Z.)
[2] Division of Energy Technology, Department of Space, Earth and Environment, Chalmers University of Technology, 41296 Gothenburg, Sweden
[3] Research Institute for Coal Clean and Efficient Utilization, College of Electric Power, North China University of Water Resources and Electric Power, Zhengzhou 450045, China; david-wn@163.com
[4] State Key Laboratory of High-Efficiency Utilization of Coal and Green Chemical Engineering, Ningxia University, Yinchuan 750021, China; majingjing@nxu.edu.cn
* Correspondence: daofeng.mei@chalmers.se

Abstract: Combining iron and copper ores can generate an oxygen carrier that has a synergic effect of high temperature resistance and high reactivity. In this work, typical cements available in the market were studied as binders to bind magnetite and chalcopyrite to develop a suitable oxygen carrier for chemical-looping combustion (CLC). A first selection step suggested that an aluminate cement, namely CA70, could favor the generation of oxygen carrier particles having good crushing strength, good particle yield, and high reactivity. The CA70-bonded oxygen carrier was then subjected to cyclic tests with CH_4, CO, and H_2 in reduction and in air oxidation at temperatures of 850, 900, and 950 °C with gas concentrations of 5, 10, 15, and 20% in a batch-fluidized bed reactor. The increase in temperature promoted the fuel conversion. At 950 °C, the conversions of CH_4 and CO reached up to 80.4% and 99.2%, respectively. During more than 30 cycles, the oxygen carrier kept a similar reactivity to the fresh carrier and maintained its composition and physical properties. The oxygen transport capacity was maintained at 21–23%, and the phases were CuO, Fe_2O_3, Al_2O_3, and minor CaS. In the used sample, some grains were observed, but the morphology was not greatly changed. Agglomeration was absent during all the cycles, except for the deep reduction with H_2.

Keywords: chemical-looping combustion; oxygen carrier; copper ore; iron ore; cement binder

Citation: Li, M.; Zheng, T.; Mei, D.; Wang, B.; Ma, J. Selecting and Testing of Cement-Bonded Magnetite and Chalcopyrite as Oxygen Carrier for Chemical-Looping Combustion. *Energies* **2022**, *15*, 5093. https://doi.org/10.3390/en15145093

Academic Editor: Arturo Cabello

Received: 6 June 2022
Accepted: 8 July 2022
Published: 12 July 2022

1. Introduction

Chemical-looping combustion (CLC) provides a novel carbon capture technology, which has the property of inherently separating CO_2 from combustion air and, thus, requiring low energy for CO_2 capture [1]. In CLC, the fuel combustion is split into a two-step reaction in two reactors, i.e., the fuel reactor and the air reactor, as described in Figure 1. In the fuel reactor, the oxygen carrier (MO_x, transition metal oxides) provides the oxygen for fuel combustion through reaction (1), where the fuel (C_nH_{2m}) is oxidized to H_2O and CO_2. The reduced oxygen carrier (MO_{x-1}) is then conveyed to the air reactor, where the oxygen carrier reacts with air oxygen through reaction (2) to regenerate to MO_x for the next cycle. Ideally, there are only H_2O and CO_2, where the latter can be easily captured through simple condensation; thus, intensive CO_2 separation is avoided in CLC.

The fuel reactor oxygen carrier reduction with fuel is as follows:

$$(2n + m)MO_x + C_nH_{2m} \rightarrow (2n + m)\ MO_{x-1} + mH_2O + nCO_2 \quad (1)$$

The air reactor oxygen carrier regeneration is as follows:

$$(2n + m)MO_{x-1} + (n + m/2)O_2 \rightarrow (2n + m)MO_x \quad (2)$$

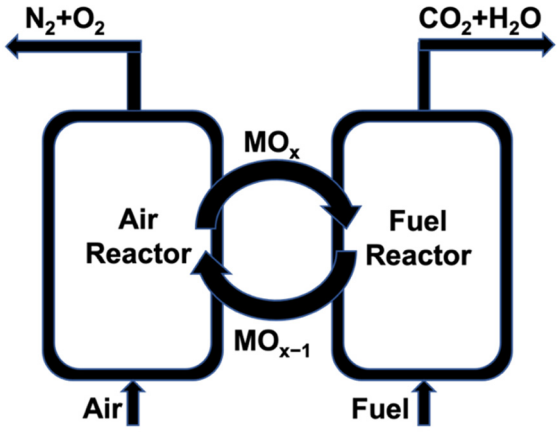

Figure 1. Schematic description of chemical-looping combustion.

The oxygen carrier is a cornerstone in CLC, as it functions to transport oxygen for fuel combustion [2]. The oxygen carrier should have properties of good reactivity, high oxygen transport capacity, environmentally benign, no toxicity, and a long lifetime [3]. In the case of large-scale, solid-fuel CLC, the ash residue from combustion needs to be removed from the system to avoid accumulation [4]. Together with the ash, loss of the oxygen carrier is inevitable. In this context, low-cost natural ores and byproducts from industrial process are preferred [5–11]. Several such materials have been demonstrated in CLC, which is equal to more than 2200 h of operations in continuous CLC systems having a thermal power of 0.5–1 MW_{th} [12,13]. Among them, copper ore showed high reactivity [14] and had potential for gas-phase O_2 release, which is a property called chemical-looping with oxygen uncoupling (CLOU) [15–17]. Actually, a study showed the property of gaseous oxygen release and solid fuel combustion with a copper ore in CLOU mode [14]. Various operation conditions were explored in this study, and slight agglomeration of the particles was noticed [14]. Studies with copper ore as an oxygen carrier investigating its agglomeration behavior were summarized in a review work [8], but recently, few reports can be found using copper ore as an oxygen carrier. A reason might be the limited accessibility of copper ore since it is less available and more expensive than iron ore and manganese ore [18–20]. On the contrary, iron ore is more available, more abundant, high-temperature resistant, and less expensive. However, it has lower reactivity than copper ore [21] since iron-based materials cannot release gaseous oxygen, and the CLC process must happen in a gas–solid reaction fashion [22]. Some methods, e.g., doping with foreign ions, were attempted to improve the performance of iron-based materials [23]. Another option is the combination of copper ore and iron ore to form a new oxygen carrier, which can benefit the synergic effect of copper and iron [21,24]. In this case, some new attempts have been carried out to combine copper ore and iron ore and redmud using a cement binder through simple mechanical mixing [25,26] or an extrusion–spheronization method [27]. In these works, aluminosilicate cements have been used to test their suitability as binders for oxygen carrier preparation from natural ores. However, in the market, there is a wide range of different types of cement, which are potential binders and need to be studied. Since these cements have different compositions, properties, and features, as well as costs, it can be an opportunity to find a less expensive and more suitable cement binder through a thorough exploration of a wide range of cements.

In this work, nine cement samples from three types are employed as binders to synthesize a magnetite-chalcopyrite oxygen carrier. The selection of the mechanical properties is based on 1400 cylindrical samples and 36 cubic samples obtained through a mold synthesis method. From this preliminary selection, an aluminate cement, called CA70, is selected as

the best candidate for the bonded oxygen carrier preparation. The CA70-bonded oxygen carrier is then subjected to cyclic tests with CH_4, CO, and H_2 in a batch-fluidized bed reactor operating under various gas concentrations and temperatures. The characterization of the fresh and used oxygen carrier is performed through techniques such as XRD, SEM, XPS, and ICP-OES to evaluate the evolution of the physical and chemical properties of the oxygen carrier before and after the CLC cycles.

2. Experimental Section

2.1. Characterization Techniques

Various characterizations were employed to study the physical and chemical properties of the samples involved in the current work. X-ray diffraction (XRD) analysis was used to study the crystal phases of fresh and used samples. This analysis was carried out with a D8ADVANCE polycrystalline X-ray diffractometer, and the scanning range was 2θ = 5–85° with a step size 0.02°. The equipment was operated under Cu kα radiation (λ = 1.5418 Å), a voltage of 40 kV, and a current of 40 mA. Particle surface and morphology of the samples were analyzed through a scanning electron microscopy (SEM) technique with an Apreo C HiVac scanning electron microscope. Element contents (Fe, Cu, Al, Mg, Ca, and S) in the samples were determined through an inductively coupled plasma-optical emission spectrometry (ICP-OES) analysis with an ElementAl analysis Agilent725 instrument. Surface ions (Fe^{2+}, Fe^{3+}) of the samples were analyzed with a VG multilab 2000 X-ray photoelectron spectroscopy (XPS) analyzer. The particle size distribution of the oxygen carrier samples was detected with a Winner2008A laser particle size analyzer. Crushing and cutting strength tests was performed using a Food Technology TMS-Pro strength tester, while the crushing strength of the particles was determined by fracturing 20 randomly selected particles with a Nidec-Shimpo FGJ-5 dynamometer. The bulk density of the particles was measured by weighing a known volume of sample following a WHO standard method [28,29]. The reactivity and oxygen transport capacity of the oxygen carriers were analyzed with a thermogravimetric analyzer (TGA) at 950 °C in a reducing atmosphere of 15% CO with 20% CO_2 or 15% H_2 balanced with N_2, as well as in an oxidizing atmosphere of 100% air.

2.2. The Magnetite, Chalcopyrite, and Cements

A magnetite iron ore (Ekou, Shanxi Province) and a chalcopyrite copper ore (Zhongtiaoshan, Shanxi Province), which both were crushed and sieved to a size smaller than 106 μm, were used as the active parts of the oxygen carrier in the current work. The compositions of these ores are shown in Table 1, where it is seen that the magnetite had mainly Fe_3O_4, and the chalcopyrite had $CuFeS_2$, FeS_2, and $Cu_4Fe_5S_8$ as the major phases. After high-temperature treatment, the chalcopyrite could be oxidized to mainly CuO. The CuO and Fe_3O_4 were both active components for the oxygen carrier in the CLC process. In fact, iron ore was tested and demonstrated previously as an oxygen carrier [30]. In addition, chalcopyrite was tested with an anthracite coal in a batch-fluidized bed reactor [14]. The magnetite showed a medium reactivity and high resistance against agglomeration, whereas the chalcopyrite exhibited high reactivity but tended to agglomerate when the temperature was more than 950 °C. The combination of these ores can generate a bimetallic oxygen carrier and lead to a synergy effect, as well [21,26].

Table 1. Phase composition of the magnetite and chalcopyrite.

Name	Type	Main XRD Phase
Magnetite	Fe-ore	Fe_3O_4
Chalcopyrite	Cu-ore	$CuFeS_2$, FeS_2, $Cu_4Fe_5S_8$

Cement, a common construction material, was proved as a good candidate for binding copper and iron ores to form an oxygen carrier for the CLC process [25]. However, in

that work, only one cement was tested, but there are many types of commercial cement in the market. In this work, 9 cement samples from 3 categories (Portland, aluminate, and sulfoaluminate cement), which are available at a commercial scale, were tested as binders for synthesizing the magnetite-and-chalcopyrite oxygen carrier. As seen in Table 2, the Portland cement (PO32.5R, PO42.5, and PO52.5) had XRD phases from the Ca-Si-O system, the aluminate cement (CA50–A600, CA50–A700, CA50–A900, CA70, and CA80) compositions were mainly based on the Ca-Al-O system, and the sulfoaluminate cement (SA42.5) had Ca_2SiO_4, $CaSO_4$, and $Ca_4Al_6SO_{16}$ as the major phases.

Table 2. Cements and compositions.

Category and Type		Main XRD Phase
Portland	PO32.5R	Ca_2SiO_4, Ca_3SiO_5
	PO42.5	Ca_3SiO_5, SiO_2
	PO52.5	Ca_3SiO_5, SiO_2
Aluminate	CA50-A600	$CaAl_2O_4$, $Ca_2Al_2SiO_7$, $CaAl_4O_7$
	CA50-A700	$CaAl_2O_4$, $Ca_2Al_2SiO_7$, $CaAl_4O_7$
	CA50-A900	$CaAl_2O_4$, $Ca_2Al_2SiO_7$, $CaAl_4O_7$
	CA70	$CaAl_4O_7$, $CaAl_2O_4$
	CA80	Al_2O_3, $CaAl_2O_4$, $CaAl_4O_7$
Sulfoaluminate	SA42.5	Ca_2SiO_4, $CaSO_4$, $Ca_4Al_6SO_{16}$

2.3. Cement-Bonded Magnetite-Chalcopyrite Samples

2.3.1. Cylinder Samples for Preliminary Selection

Cement hardening is a crucial step for combining magnetite and chalcopyrite ores, as this step involves a hydration reaction that is usually quite slow and can be time-consuming for large-scale oxygen carrier manufacture. Cylinder-shaped samples were prepared to study the effect of aging time and to optimize the hydration reaction. The nine cements shown in Table 2 were used as binders for the preparation of magnetite-chalcopyrite samples through mechanical mixing and a mold method. In the mixture, the mass ratio chalcopyrite/magnetite was fixed to 2/8, according to previous works [21,25], while the proportion of cement was set to 20%. Water was added during the mixing, and its amount corresponded to a water/cement ratio of 1.65/1. After thorough stirring of the mixture of cement, water, magnetite, and chalcopyrite, the obtained slurry was poured into a cylindrical mold with length geometry of "diameter × height" of "Φ × H = 4 × 4 mm" to prepare cylinder samples, as shown in Figure 2. The mixture was placed in the mold and dried at room temperature under a natural atmosphere for 10 periods (0.5–12 days), where the 12th day corresponded to a hydration time for complete hardening of the cement, and the rest periods were used to find optimal hydration and aging time for the oxygen carrier preparation.

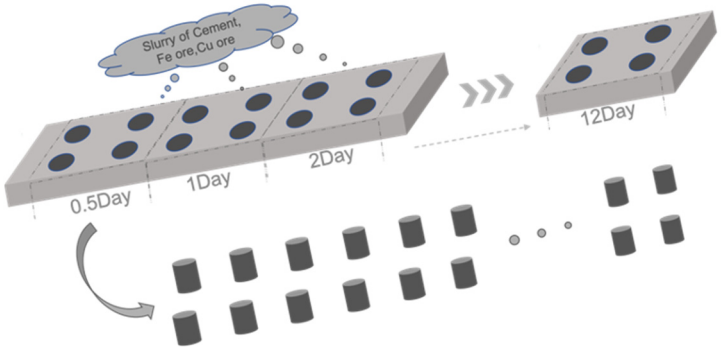

Figure 2. Preparation of cylindrical cement-bonded magnetite-chalcopyrite samples based on various aging and hydration time (0.5 day, 1 day, 2 days, 3 days, 4 days, 5 days, 6 days, 8 days, 10 days, and 12 days).

2.3.2. Cubic Samples for Secondary Selection

The preliminary selection based on cylindrical samples suggested that CA70- and SA42.5-bonded materials had the highest mechanical performances before calcination (detailed below in Section 4.1.1); meanwhile, PO32.5R was the most common cement and had the lowest price in the market. Therefore, these three cements were further considered in this section for the secondary selection, where the high-temperature calcination performance was mainly focused. Since a larger amount of particles was required in this step of selection, a cubic mold with a bigger volume (with "length × width × height" of "30 × 30 × 30 mm", see Figure 3) was used for sample preparation. In total, eighteen sets of samples were prepared with a period of 0.5–6 days of natural drying (hydration reaction).

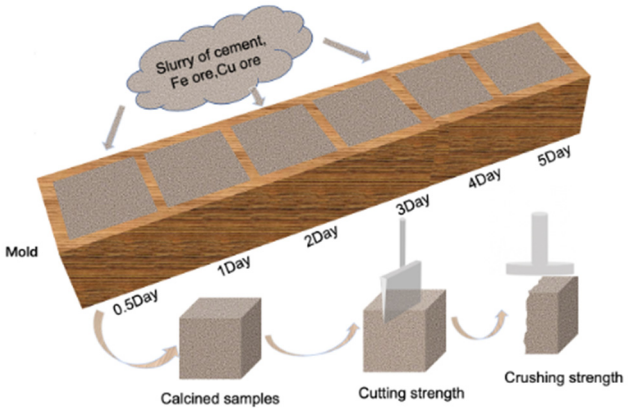

Figure 3. Preparation of cubic cement-bonded samples and cutting and crushing strength tests of the calcined samples with varying aging durations (0.5 day, 1 day, 2 days, 3 days, 4 days, and 5 days).

2.4. The CA70-Cement-Bonded Oxygen Carrier

Based on the preliminary and secondary selections, the CA70 cement was considered as the best binder for the magnetite-chalcopyrite oxygen carrier preparation, which is detailed below in Section 4.1.1. Thus, the copper ore weight percentage was set to 20 wt.%, while the iron ore amount was 80 wt.%, and the weight percentage of cement was 20 wt.% of the total solids mass. After being fully uniformed under continuous stirring, the mixture was poured into the cubic mold and naturally dried for two days (48 h). Different from the cylindrical samples, the cubic blocks were dried and placed in a muffle furnace to calcine at 500 °C for 5 h, and then 1000 °C for 10 h, to study the effect of calcination. After cooling down to room temperature, the calcined cubic samples were crushed and sieved to 106–300 μm particles, which were used as oxygen carriers in the current work. The main properties of the oxygen carrier are presented in Table 3, where the XRD phase, oxide content, oxygen transport capacity, bulk density, and crushing strength are shown. After calcination, the sulfur that originated from the chalcopyrite was not completely discarded, as CaS was detected. The crushing strength was 2.27 N, which is sufficient for use in fluidization systems [31].

Table 3. Characterizations and properties of the CA70-bonded oxygen carrier.

XRD Phase	Fe_2O_3, CuO, $Ca_2Al_2SiO_7$, $CaSO_4$
Fe_2O_3, CuO (wt.%)	42, 2.73
Roc (wt.%)	23
Particle size (μm)	106–300
Bulk density (g/cm^3)	1.65
Crushing strength (N)	2.27

2.5. Batch-Fluidized Bed Experiments

The reduction–oxidation cycle in the CLC process was simulated in a batch-fluidized bed reactor by switching the reacting environment between reduction (CH_4, CO, and H_2) and oxidation (air) under various temperatures (850, 900, and 950 °C) and gas concentrations (5, 10, 15, and 20%). A schematic description of the reactor is displayed in Figure 4. The reactor was made from high-temperature stainless steel and heated by a surrounding high-temperature furnace. Fluidizing, reacting gases and water steam entered the reactor from the bottom. After reacting with and passing through the bed material, the gas stream left from the reactor top, where low-granulometry particles were filtered with two identical filters. Afterward, the gas stream was cooled down by a cooler and then led to a gas analyzer to determine the gas concentration or passed through the stack before being emitted to the atmosphere. The gas analyzer (Gasboard-3100, Hubei Ruiyi Automatic Control System Co., Ltd., Wuhan, China) could measure the concentrations of CO, CO_2, CH_4, H_2, and O_2, and these concentrations were collected by a data logger and registered to a computer at a rate of one point per second. The performance of the oxygen carrier was studied by the reactions with CH_4, CO, and H_2 in the reduction step, while the gas concentration was varied from 5, 10, 15, and 20%. The lowest concentration (5%) was not used with CO and H_2 because of their high reactivity, which could lead to full conversion of these gases and was, thus, not convenient for data processing, as detailed below in Section 3. In the case of CH_4 and H_2, water steam was mixed with up to 50% H_2O with the fuels, whereas in the case of CO reduction, 20% CO_2 was mixed. The H_2O and CO_2 were used to either avoid carbon deposition from CH_4 and CO or to prevent deep reduction of the oxygen carrier in the cases of agglomeration and defluidization [32]. The total gas flow rate was kept at 200 L/h for both reduction and oxidation. An amount of 300 g of the CA70-bonded magnetite-chalcopyrite oxygen carrier was used as the bed. Three temperatures (850, 900, and 950 °C) were used to study the effect of temperature. In most of the experiments, ten cycles were performed under each reacting condition, and in total, more than 30 cycles were iterated.

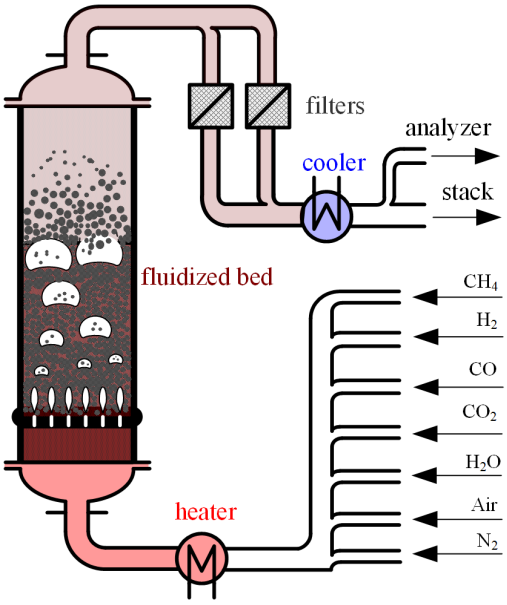

Figure 4. Batch-fluidized bed reactor setup.

3. Data Evaluation

In the reduction with CH_4 and CO, the gas conversion to CO_2 was calculated and used to evaluate the gas reactivity with the oxygen carrier. In the H_2 experiments, all the H_2 was

converted to steam, which however, was not measured; thus, the H_2 conversion was not calculated. The gas conversion for CH_4 and CO was calculated with the following formulas:

$$X_{(CH_4)} = \frac{C_{CO_{2,out}}}{C_{CO_{2,out}} + C_{CO,out} + C_{CH_{4,out}}} \quad (3)$$

$$X_{(CO)} = \frac{C_{CO_{2,out}}}{C_{CO_{2,out}} + C_{CO,out}} \quad (4)$$

where $X(i)$ is the conversion of gas i (i = CH_4 or CO), and $C_{i,out}$ is the gas concentration of i (CH_4, CO, or CO_2) measured with the gas analyzer.

The oxygen carrier reactivity was evaluated using a mass-based conversion of the bed, which was calculated based on the measured gas concentration and oxygen balance during the reactions. The mass-based conversion during the CH_4, CO, and H_2 experiments was calculated through the equations below:

$$\omega_{CH_4} = 1 - \int_{t_0}^{t} \frac{n_{out} M_O}{m_{ox}} (4C_{CO_{2,out}} + 3C_{CO,out} - C_{H_{2,out}}) dt \quad (5)$$

$$\omega_{CO} = 1 - \int_{t_0}^{t} \frac{n_{out} M_O}{m_{ox}} C_{CO_{2,out}} dt \quad (6)$$

$$\omega_{H_2} = 1 - \int_{t_0}^{t} \frac{M_O}{m_{ox}} (n_{in} C_{H_2,in} - n_{out} C_{H_2,out}) dt \quad (7)$$

$$n_{out} = \frac{n_{N_{2,in}}}{1 - \sum_i C_i} \quad (8)$$

$$n_i = n_{out} \cdot C_i \quad (9)$$

where ω_i is the mass-based conversion during the reaction between the oxygen carrier and gas i (i = CO_2, CO, CH_4, H_2 or O_2), n_{in} is the molar flow rate of the inlet gas, n_{out} is the molar flow rate of the dry gas leaving the reactor, m_{ox} is the mass of the oxygen carrier in the bed, and M_O is the molar mass of an oxygen atom.

4. Results and Discussion

4.1. Screening of the Cement Binder

4.1.1. Crushing Strength of the Cylindrical Samples

Four cylindrical samples were obtained each day (see Figure 2), and these samples were all subjected to crushing strength tests; thus, the average value of the four cylinders was used as the crushing strength for evaluation. Figure 5 shows the crushing strength of the nine cement-bonded materials as a function of aging time. It is seen that, with the increase in drying time (or aging time), the crushing strength of the samples showed an upward trend. In particular, among all the cements, the crushing strength of the cylinders bonded by CA70 and SA42.5 increased the most rapidly as a function of the aging time studied. The crushing strengths of these two samples already became higher than 10 N after two days of aging. Following 4 days of aging, the crushing strengths of the cylinders approached stable values of around 40 N and 15 N for CA70 and SA42.5, respectively. The big variation in the crushing strength might be a result of the wide range of netting force from the different components formed during the aging period with the cements. In addition, the PO32.5R cement is the most widely used in engineering and industry, as well as having the lowest market price. Therefore, these three cements, CA70, SA42.5, and PO32.5R, were all used in the secondary selection based on cubic samples, as discussed in the next section.

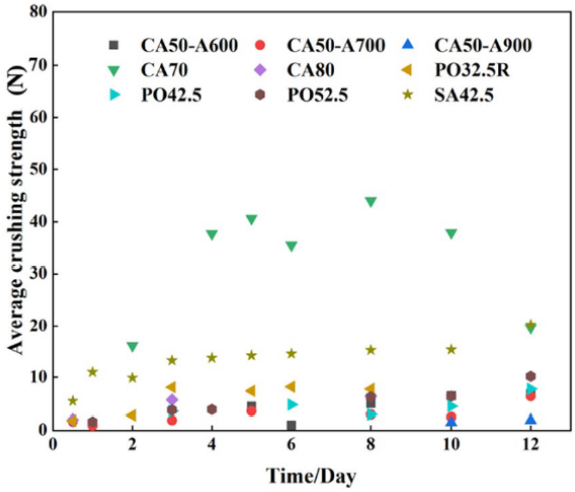

Figure 5. Crushing strengths of the cylindrical samples as a function of aging time for different cements.

4.1.2. Cement Selection Based on Cubic Samples

Cutting and Crushing Strength of the Cubic Samples

The cubic samples obtained through the method described in Section 2.3.2 were calcined (500 °C for 5 h; then, 1000 °C for 10 h), cooled down, and then subjected to a cutting strength test. The cutting strength test was performed on a complete cubic sample and could reflect the binding strength between the raw fine particles; thus, it was considered as an indicator for the preliminary selection of the cement binders. After the cutting strength test, the samples were broken into two half-cubes, which were then used to test the crushing strength. Therefore, a total of 36 strength tests were conducted for 18 groups of samples, (three cements by six aging periods). The cutting strengths and crushing strengths are shown in Table 4. As compared to the crushing strength, most of the samples showed smaller cutting strength values. Among the three cements, the crushing strengths and cutting strengths of the CA70-bonded samples were the highest, and the values were all beyond the upper limit of the dynamometer, i.e., greater than 980 N. However, the samples bonded with the PO32.5R and SA42.5 cements had relatively smaller cutting strengths and crushing strengths.

Table 4. Cutting strengths and crushing strengths of the cubic samples using various cements as binders.

Dry Time (Day)	Cement Type	0.5	1	2	3	4	5
Cutting strength (N)	PO32.5R	654.2	691.2	349.1	762.6	>980	235
	CA70	>980	>980	>980	>980	>980	>980
	SA42.5	355.8	405.7	157.6	460	153.3	128.2
Crushing strength (N)	PO32.5R	>980	>980	>424.7	>980	>980	>980
	CA70	>980	>980	>980	>980	>980	>980
	SA42.5	696.7	713	>980	791	364.7	396.8

Particle Yield and Particle Crushing Strength

The crushed cubic samples from the above cutting and crushing strength tests were then smashed with an electric crusher using the same procedure and then sieved with stainless steel sieves to 106-300 μm. During the crushing, the gap between the crusher plates was fixed, and the cubic samples were passed through the crusher only once to try to maintain the same procedure for all the samples. Figure 6a shows the mass-based yield of particles with sizes from 106–300 μm. The yield increased as a function of aging time before 50 h and then became stable afterwards. It is clear that the CA70-bonded sample

had the highest yield, i.e., around 16–20 wt.%, after around 48 h of aging and calcination, while PO32.5 and SA42.5 shared a similar yield of around 10 wt.%. Figure 6b displays the crushing strength of the particles, and there was not a clear tendency of crushing strength variation over aging time. However, the crushing strength of the CA70-bonded particles peaked around 1.2 N after 48 h of aging and calcination at 1000 °C.

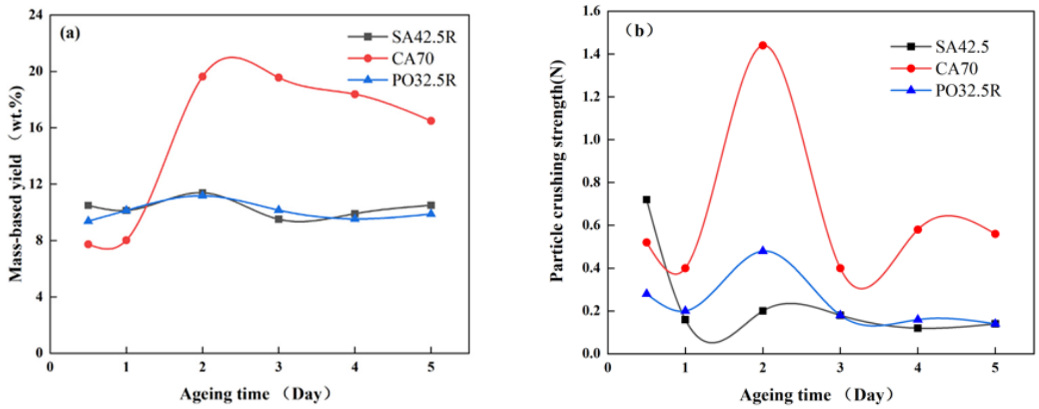

Figure 6. Comparison of the CA70, SA42.5, and PO32.5R cement-bonded oxygen carriers during the aging of the cubic samples: (**a**) mass-based yield of particles having sizes from 106–300 µm and (**b**) crushing strength of particles with sizes ranging from 106–300 µm.

4.1.3. Reactivity Comparison in TGA

The CA70, SA42.5, and PO32.5R cement-bonded oxygen carrier particles were also subjected to reactivity tests with CO in TGA. Figure 7 shows the weight loss of these oxygen carriers during reduction in TGA. All these samples had a final weight loss of around 87%, which suggested very similar oxygen transport capacities of the oxygen carriers. On the contrary, the reactivity with CO was different among the CA70-, SA42.5-, and PO32.5R-bonded oxygen carriers. The CA70-bonded sample had the highest reactivity, i.e., showing the steepest slope of the curve between 100–200 s. Therefore, the CA70-bonded particles were selected for further reactivity tests with various gases in the batch reactor.

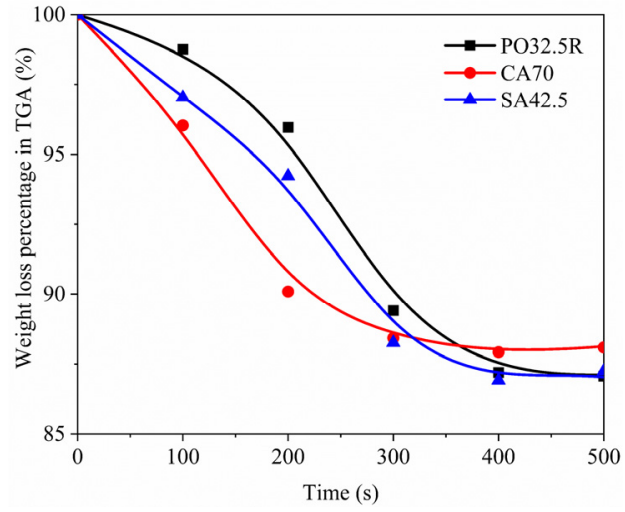

Figure 7. Percentages of weight loss of PO32.5R, CA70, and SA42.5 cement-bonded oxygen carriers in the TGA tests with 15% CO and 20% CO_2 balanced by N_2 at 950 °C.

4.2. Performance of Oxygen Carrier in the Batch Reactor

4.2.1. Reaction Progress with CH_4, CO, and H_2

Figure 8 shows an example of the reaction progress of the CA70-bonded oxygen carrier with CH_4, CO, and H_2 at 85 °C. As the reduction with CH_4 started, the concentration of

CH_4 increased rapidly to a peak around 20%, which indicated the slippage of CH_4, probably through gas bypass in the bubbles rising from the dense zone of the fluidized bed [33,34]. Afterwards, this decreased gradually to about 5% from 200–600 s, while the CO_2 was relatively stable at around 30%. In the cases of CO and H_2, in the initial stages of reduction, i.e., 0–200 s and 0–300 s, respectively, the fuel components were completely converted. Therefore, the CO and H_2 were more reactive than CH_4 with the same bed amount. Thus, the rate of oxygen carrier conversion, i.e., the slope of the blue triangle labelled ω-t curve, with H_2 was significantly higher than CO and CH_4. However, after reacting with H_2, the bed agglomerated due to the high extent of the reduction. The tests with H_2 at other temperatures were cancelled, and only data for the CO and CH_4 experiments are shown and discussed below.

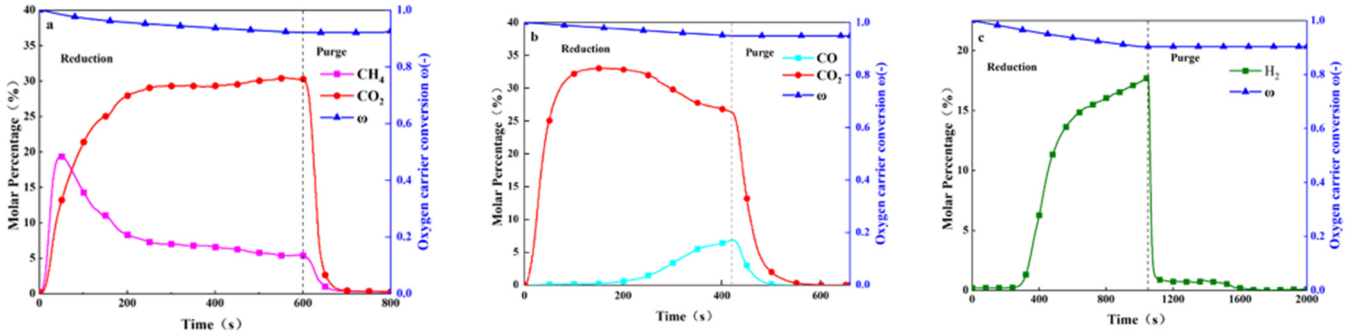

Figure 8. Typical reaction progress of the CA70-bonded oxygen carrier at 850 °C with (**a**) 20% CH_4, 20% H_2O, and 60% N_2; (**b**) 20% CO, 20% CO_2, and 60% N_2; and (**c**) 20% H_2, 50% H_2O, and 30% N_2.

4.2.2. Influence of Temperature

Three temperatures (850, 900, and 950 °C) were used to study the influence on the combustion performance, as seen in Figure 9. Although the CH_4, CO, and H_2 were all tested at these three temperatures, the H_2 experiments are not shown here, as agglomeration occurred, as stated above in Section 4.2.1. In the case of the CH_4 experiments, the CH_4 concentration showed an overall upward trend at the three temperatures. The difference was that the CH_4 concentration rose rapidly at 850 °C, and this indicated that the reactivity was not enough to completely convert the CH_4 at this temperature. This was similar for the reaction at 900 °C; however, when the temperature was raised to 950 °C, the CH_4 increased much more slowly, displaying a much better conversion of CH_4. With the progress of the reaction, the CO_2 concentration in the outlet gas was kept above 8%, which was close to the theoretical value of 10% for complete CH_4 conversion. Meanwhile, the CH_4 concentration was kept below 2%. In the CO experiments, reduction with a gas mixture composed of 20% CO, 20% CO_2, and 60% N_2 was employed for evaluation. As seen in Figure 9b, when the temperature was 850 °C, the CO concentration was initially zero, and it started to rise at 100 s. At 900 °C, the time for CO concentration rising was 180 s, which was 80 s slower than that at 850 °C. When the temperature was further increased to 950 °C, it was hard to observe residual CO in the whole reduction stage, and the concentration of CO_2 was almost unchanged after reaching the peak value. Therefore, the temperature increase improved the reaction rate and enhanced CO conversion. The positive effect of temperature is also seen in Figure 9c with fuel conversion. Here, it can also be found that the CO had a much better conversion than CH_4 at all three temperatures.

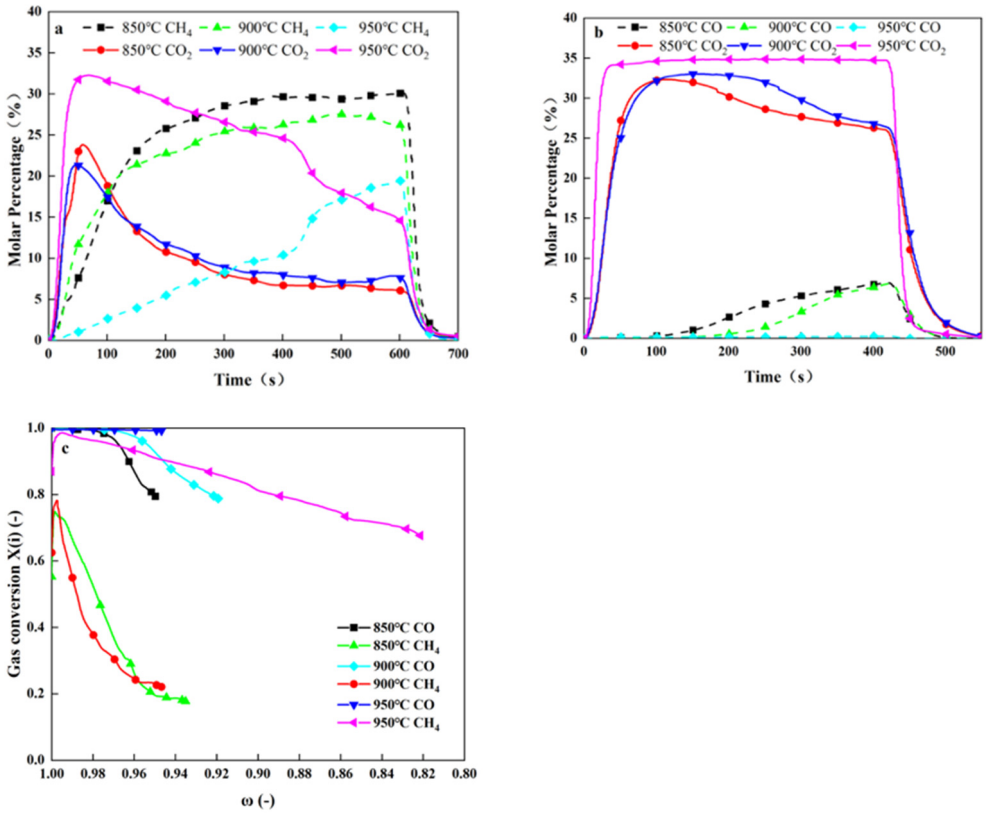

Figure 9. Effect of temperature on the reaction performance of CA70-bonded oxygen carrier: (**a**) CH_4 and CO_2 concentration curves in CH_4 experiments, (**b**) CO and CO_2 concentration curves in CO experiments, and (**c**) fuel conversion. 20% CH_4 for methane experiments, and 20% CO for carbon monoxide experiments.

4.2.3. Influence of Fuel Concentration

Figure 10 shows the effect of fuel concentration at 950 °C using CH_4 and CO as the reducing gases. In the case of the CH_4 fuel, the concentration of CH_4 was varied at 5, 10, and 20%. It can be seen from Figure 10a that the concentration of CO_2 in the whole reduction stage with 5% CH_4 was relatively stable, and the whole process had a very high methane conversion. However, the CO_2 concentration in the cases of 10% and 20% CH_4 decreased gradually with the reduction stage, and the CH_4 concentration at the reactor outlet increased gradually from 0 to 12% for 10% CH_4 and from 0 to 20% for 20% CH_4. However, the fuel conversion showed a slightly different trend, as the CH_4 concentration was varied. The level of 5% CH_4 had the highest fuel gas conversion, with 20% CH_4 having the middle gas conversion amount, whereas 10% CH_4 had the lowest conversion. In Figure 10b, the uses of 10, 15, and 20% CO as fuel also showed an effect on the gas distribution. The higher CO the concentration, the higher the CO_2 detected and the more residual CO in the reactor exit. However, in general, the fuel conversion was always equal to 1, especially when the oxygen carrier conversion value was higher than 0.92 when more oxygen was available in the oxygen carrier. The effect of fuel concentration on the gas conversion was a result of the fuel-to-oxygen carrier ratio. In general, the higher the fuel concentration, the lower the ratio and, thus, less fuel is converted. Therefore, the increase in gas concentration is usually accompanied with less fuel conversion. The 10% CH_4 was an exception, which could be attributed to artificial errors during the experiments.

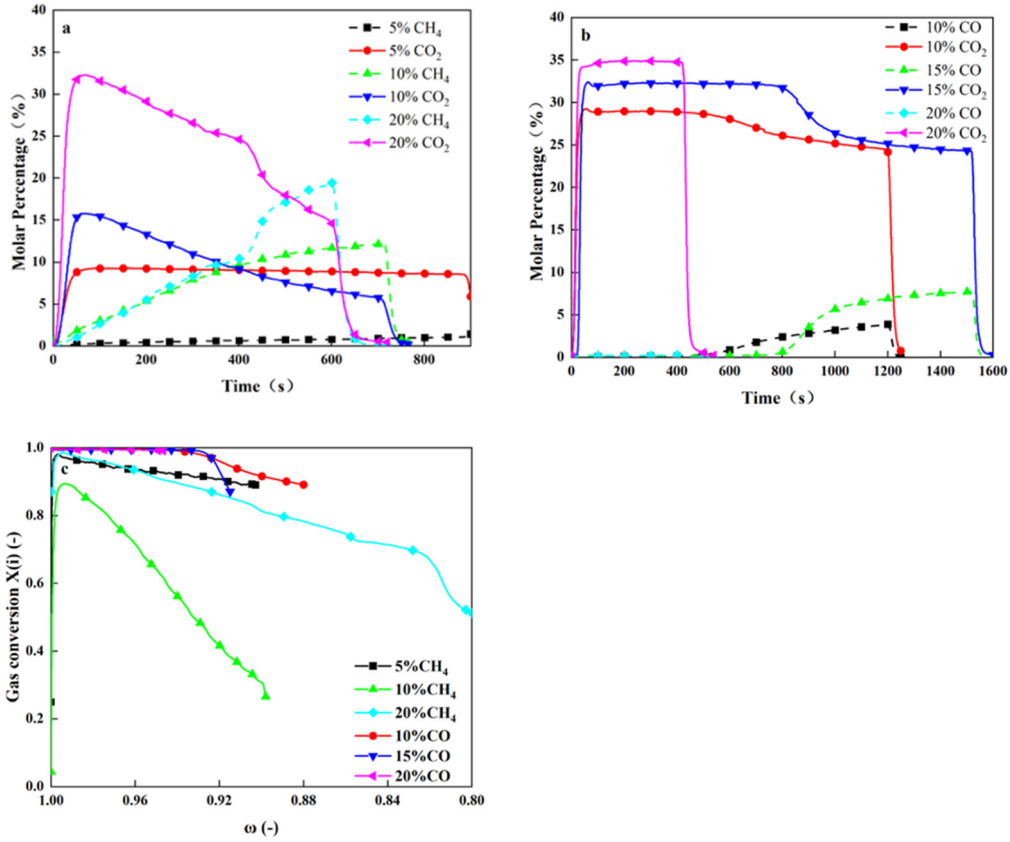

Figure 10. Effect of gas concentration on the combustion performance with CH_4 and CO, comparing (**a**) CH_4 and CO_2 concentration curves in CH_4 experiments, (**b**) CO and CO_2 concentration curves in CO experiments, and (**c**) gas conversion at three concentrations in CH_4 and CO experiments.

4.2.4. Cyclic Stability of the CA70-Bonded Oxygen Carrier

The stability of the oxygen carrier reactivity was compared with the rate of oxygen carrier conversion in the cycles, as seen in Figure 11. In all the cycles shown in the figure, the reactivity of the oxygen carrier was quite similar to the first cycle, where the oxygen carrier was considered fresh. In particular, the CH_4 cycle had an oxygen carrier conversion rate of 1.0–1.3 $\times$ 10^{-4} 1/s, excepting cycle 5 where the rate was higher than the other cycles. This could be considered as an artificial error, considering that the other cycles had a very similar rate of conversion. The stability of the oxygen carrier reactivity was also found in the cycles with CO, as seen in Figure 11b, where the reactivity was around 1.3 $\times$ 10^{-4} 1/s for all the cycles shown.

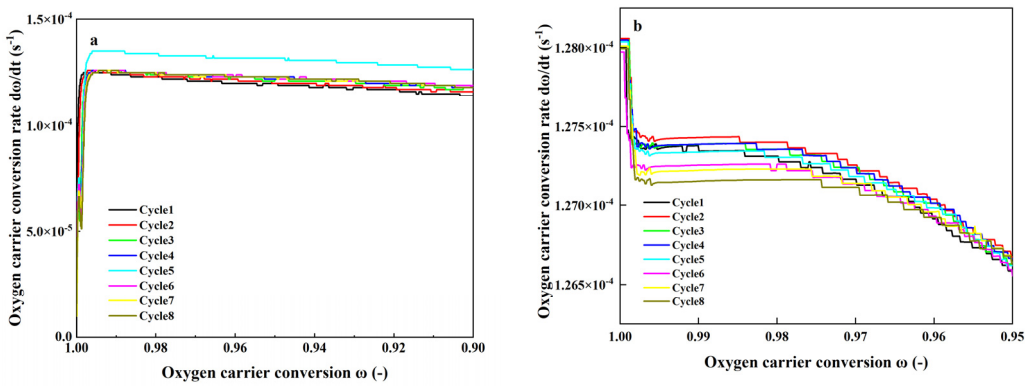

Figure 11. Rate of oxygen carrier conversion during cycles with (**a**) CH_4 and (**b**) CO at 950 °C, and the fuel concentrations were all at 5%.

4.3. Thermogravimetric Analysis for Fresh and Used Oxygen Carrier

Before the cycles in TGA started, i.e., temperature-ramping period, it was noted that the weight of the oxygen carrier decreased slowly when the temperature was increased to 950 °C. This could be attributed to the oxygen uncoupling behavior of CuO in the oxygen carrier, i.e., the gaseous O_2 release at high temperatures under an N_2 environment. However, the intensity of the O_2 release was not high, which meant that oxygen uncoupling was not relevant for this material. Typical TGA curves for the reaction between H_2 and the CA-70-bonded oxygen carrier before and after the batch reactor experiments are shown in Figure 12. With the increase in cycle number, the reduction extent of the fresh oxygen carrier tended to decrease, which meant there might be some structure reconstruction, a normal phenomenon observed with a synthetic Cu-based oxygen carrier [16]. This could be a result of Cu–Al interactions during the tests. For the used oxygen carrier samples, the degradation of the oxygen transport capacity was not obvious. Despite the degradation of the oxygen transport capacity, the reactivity of the oxygen carrier was not changed, as the slopes observed from the TGA curves in the reduction periods were similar. In the final cycle, it can be seen that both the fresh oxygen carrier and the used oxygen carrier kept high oxygen transport capacities, i.e., 23% and 21%, respectively.

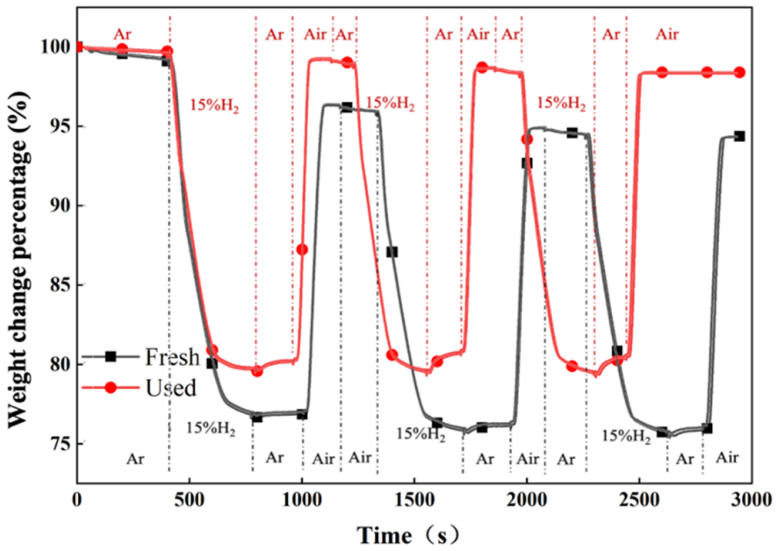

Figure 12. Thermogravimetric curves of fresh and used oxygen carriers at 950 °C, cycles with 15% H_2 in reduction, Ar in inert, and air during oxidation.

4.4. XRD and XPS Analyses

The crystal phase compositions of the fresh and used oxygen carriers were identified using an XRD technique and are shown in Figure 13. The active components of both the fresh and used samples were mainly Fe_2O_3 and CuO, while the inert components were Al_2O_3 and SiO_2. A small fraction of CaS was also detected, and this component was also active in the CLC process through the redox pair $CaSO_4$/CaS; however, due to its low amount, it was considered not relevant for CLC in the current work. Further comparison of the phases suggested that the crystal phase compositions of fresh and used oxygen carriers had changes in the SiO_2. The used oxygen carrier had a higher intensity of SiO_2 compared to the fresh sample, and this could be partly related to the possible structure rearrangement of the material after cycles in the reactor.

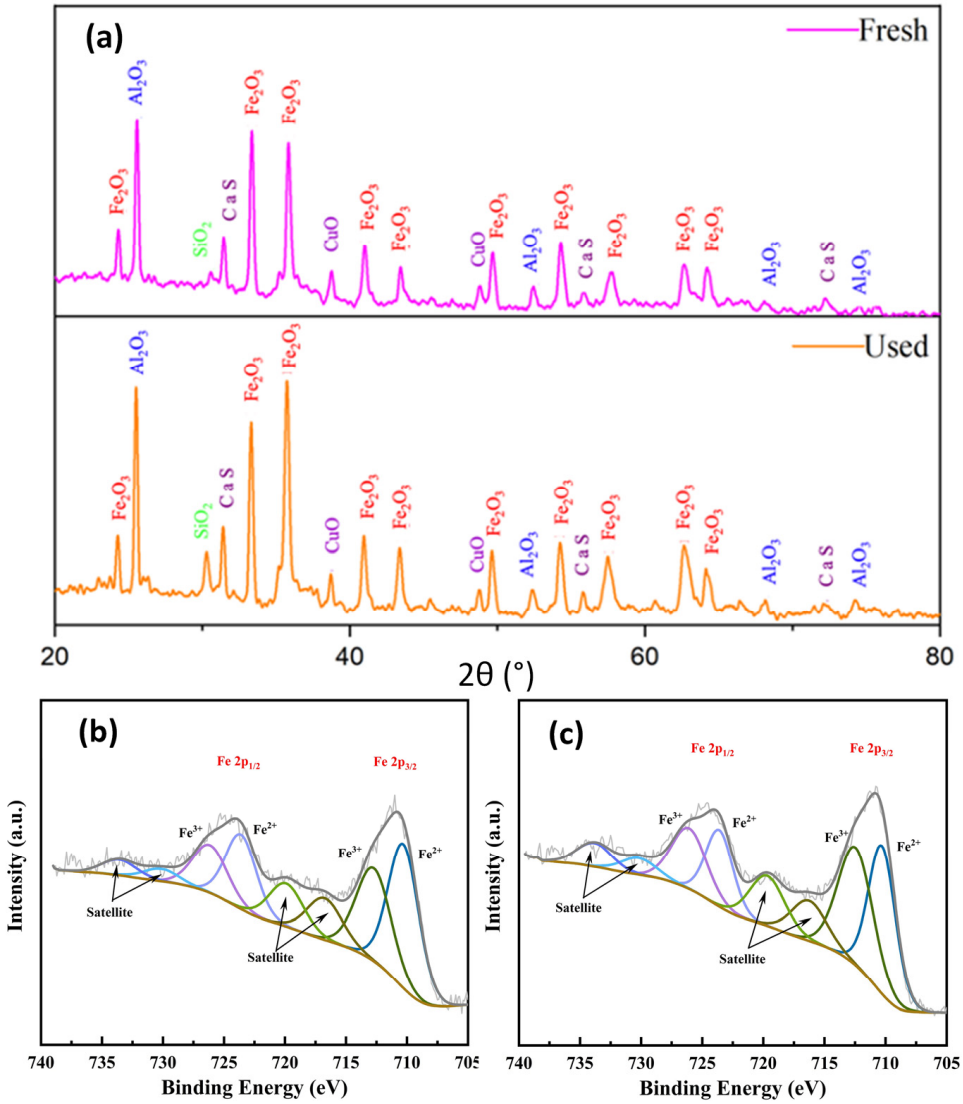

Figure 13. Comparison of the compositions of the fresh and used oxygen carriers: results from (**a**) XRD analyses of fresh and used oxygen carriers, (**b**) XPS analysis for the fresh sample, and (**c**) XPS analysis for the used sample.

The trivalent and divalent iron contents of the fresh and used oxygen carriers were obtained through XPS characterization and are compared in Figure 13, while the copper ions were not measured. However, there was little change in both of the irons before and after the reaction, which also reflected the stability of the oxygen carrier composition and was, thus, probably one reason for the stable reactivity of the oxygen carrier.

4.5. Evolution of Elements and Morphology

Figure 14 shows the contents of Ca, Fe, Cu, Mg, S, and Si in the fresh and used oxygen carriers determined with an ICP-OES technique. In the fresh sample, the iron content was around 42%, and the copper was around 3%. In the case of the used oxygen carrier after 30 cycles, the content of Cu stayed at the same level as that in the fresh sample, whereas the Fe increased to around 54%. This might be a result of the losses in oxygen or sulfur during the cycles and, as indicated in Figure 12, the change in the oxygen transport capacity from 23% to 21%.

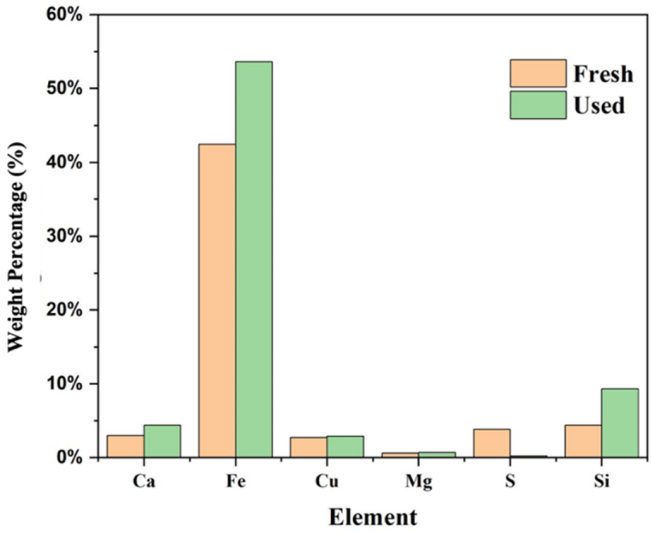

Figure 14. Element contents of the fresh and used CA70-bonded oxygen carriers.

Figure 15 displays the morphologies of the fresh and used oxygen carriers. The surfaces of fresh oxygen carriers were fluffy, and this was maintained for the used particles. A difference observed between the fresh and used particles was that, on the used particles, some grains could be found, i.e., the micrometer-scale, spheric-shaped sites on the particle's surface shown in Figure 15b. This might suggest a migration of the component from the oxygen carrier bulk to the surface during the cycles.

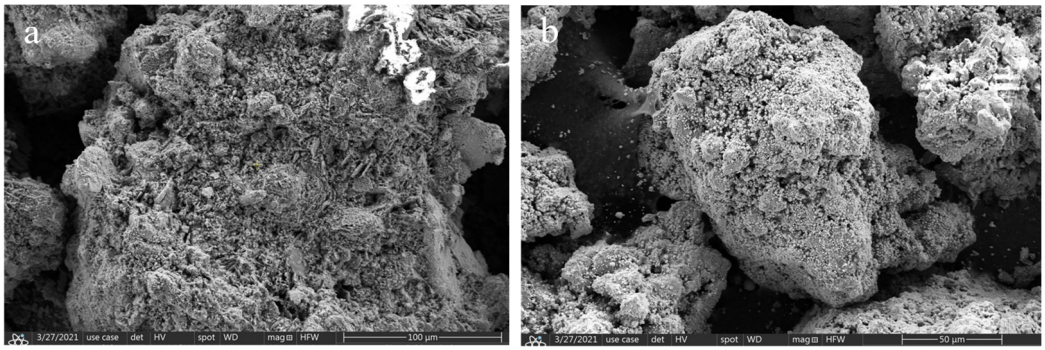

Figure 15. SEM photos of the oxygen carriers: (**a**) fresh sample and (**b**) used sample.

4.6. Particle Size Analysis

The particle size distributions of the fresh and used samples are shown in Figure 16. The particle size of the fresh oxygen carrier was basically distributed in the range of 106–300 μm, and its volume fraction decreased with the increase in particle size. After the cycles in the batch reactor, the particle size of the oxygen carrier was relatively more uniform, but parts smaller than 106 μm and larger than 300 μm increased slightly, and the average particle size of the used sample was increased from 184.1 μm for fresh material to 204.4 μm for the used material. This might be caused by the attrition that generally happens in a fluidization system. In this case, the small particles generated due to attrition were elutriated, and the remaining particles were bigger. After a size distribution test, the remaining particles in the bed had a slightly higher average particle size than the measured average before the particle size distribution test.

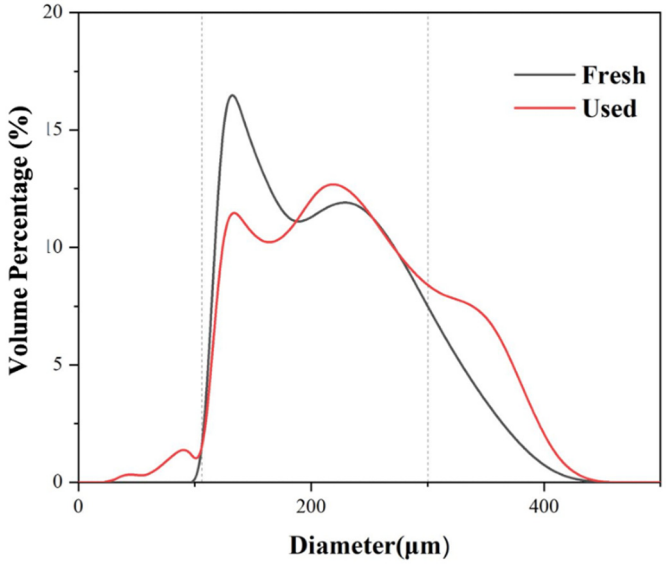

Figure 16. Particle size distributions of the fresh and used CA70-bonded oxygen carriers.

5. Conclusions

Out of the nine cements, the aluminate CA70 cement was selected as the best binder for binding magnetite and chalcopyrite to generate oxygen carrier particles that had high physical properties and reasonable reactivity. During more than 30 cyclic tests with CH_4, CO, and H_2, the CA70-bonded oxygen carrier maintained stable physical and chemical properties. The CA70-bonded oxygen carrier had an oxygen transport capacity of 21–23%, although it was slightly decreased after the cycles. The increase in temperature from 850 to 950 °C improved the reactivity between the oxygen carrier and the fuel gases. H_2 was always completely converted under the conditions studied in this work and could lead to agglomerations due to deep reduction in the bed. The conversion of CH_4 peaked at 80.4% in the cast with 950 °C and 5% CH_4. Almost all the CO was converted during the whole reduction stage. No carbon deposition was found during the cycles. Although some migrated elements were found forming grains, particle agglomeration was not observed with CH_4 and CO, where deep reduction of the oxygen carrier was not reached.

Author Contributions: Data curation, D.M.; Formal analysis, M.L.; Funding acquisition, D.M.; Investigation, M.L., T.Z., D.M., B.W. and J.M.; Methodology, D.M.; Project administration, D.M., B.W. and J.M.; Writing—original draft, M.L.; Writing—review & editing, D.M. All authors have read and agreed to the published version of the manuscript.

Funding: This research was funded by National Natural Science Foundation of China [grant number 51906083] and the State Key Laboratory Foundation for the High-Efficiency Utilization of Coal and Green Chemical Engineering [grant number 2021-K29]. And the APC was funded by these two grants.

Institutional Review Board Statement: Not applicable.

Informed Consent Statement: Not applicable.

Data Availability Statement: The data presented in this study are available on request from the corresponding author.

Conflicts of Interest: The authors declare no conflict of interest.

References

1. Lyngfelt, A.; Leckner, B.; Mattisson, T. A fluidized-bed combustion process with inherent CO_2 separation; application of chemical-looping combustion. *Chem. Eng. Sci.* **2001**, *56*, 3101–3113. [CrossRef]
2. Adánez, J.; Abad, A.; García-Labiano, F.; Gayán, P.; Diego, L.F.D. Progress in Chemical-Looping Combustion and Reforming technologies. *Prog. Energy Combust. Sci.* **2012**, *38*, 215–282. [CrossRef]

3. Adánez, J.; de Diego, L.F.; García-Labiano, F.; Gayán, P.; Abad, A.; Palacios, J.M. Selection of Oxygen Carriers for Chemical-Looping Combustion. *Energy Fuels* **2004**, *18*, 371–377. [CrossRef]
4. Lyngfelt, A.; Leckner, B. A 1000 MWth boiler for chemical-looping combustion of solid fuels—Discussion of design and costs. *Appl. Energy* **2015**, *157*, 475–487. [CrossRef]
5. Lyngfelt, A. Chemical-looping combustion of solid fuels—Status of development. *Appl. Energy* **2014**, *113*, 1869–1873. [CrossRef]
6. Mattisson, T.; Keller, M.; Linderholm, C.; Moldenhauer, P.; Rydén, M.; Leion, H.; Lyngfelt, A. Chemical-looping technologies using circulating fluidized bed systems: Status of development. *Fuel Process. Technol.* **2018**, *172*, 1–12. [CrossRef]
7. Adánez, J.; Abad, A.; Mendiara, T.; Gayán, P.; de Diego, L.F.; García-Labiano, F. Chemical looping combustion of solid fuels. *Prog. Energy Combust. Sci.* **2018**, *65*, 6–66. [CrossRef]
8. Matzen, M.; Pinkerton, J.; Wang, X.; Demirel, Y. Use of natural ores as oxygen carriers in chemical looping combustion: A review. *Int. J. Greenh. Gas Control.* **2017**, *65*, 1–14. [CrossRef]
9. Mendiara, T.; Pérez, R.; Abad, A.; de Diego, L.F.; García-Labiano, F.; Gayán, P.; Adánez, J. Low-Cost Fe-Based Oxygen Carrier Materials for the iG-CLC Process with Coal. 1. *Ind. Eng. Chem. Res.* **2012**, *51*, 16216–16229. [CrossRef]
10. Wang, Y.; Tian, X.; Zhao, H.; Liu, K. The use of a low-cost oxygen carrier prepared from red mud and copper ore for in situ gasification chemical looping combustion of coal. *Fuel Process. Technol.* **2020**, *205*, 106460. [CrossRef]
11. Song, T.; Shen, L. Review of reactor for chemical looping combustion of solid fuels. *Int. J. Greenh. Gas Control.* **2018**, *76*, 92–110. [CrossRef]
12. Lyngfelt, A. Chemical Looping Combustion: Status and Development Challenges. *Energy Fuels* **2020**, *34*, 9077–9093. [CrossRef]
13. Mei, D.; Soleimanisalim, A.H.; Linderholm, C.; Lyngfelt, A.; Mattisson, T. Reactivity and lifetime assessment of an oxygen releasable manganese ore with biomass fuels in a 10 kWth pilot rig for chemical looping combustion. *Fuel Process. Technol.* **2021**, *215*, 106743. [CrossRef]
14. Zhao, H.; Wang, K.; Fang, Y.; Ma, J.; Mei, D.; Zheng, C. Characterization of natural copper ore as oxygen carrier in chemical-looping with oxygen uncoupling of anthracite. *Int. J. Greenh. Gas Control.* **2014**, *22*, 154–164. [CrossRef]
15. Mattisson, T.; Lyngfelt, A.; Leion, H. Chemical-looping with oxygen uncoupling for combustion of solid fuels. *Int. J. Greenh. Gas Control.* **2009**, *3*, 11–19. [CrossRef]
16. Mei, D.; Abad, A.; Zhao, H.; Adánez, J. Characterization of a sol–gel derived $CuO/CuAl_2O_4$ oxygen carrier for chemical looping combustion (CLC) of gaseous fuels: Relevance of gas–solid and oxygen uncoupling reactions. *Fuel Process. Technol.* **2015**, *133*, 210–219. [CrossRef]
17. Adánez-Rubio, I.; Arjmand, M.; Leion, H.; Gayán, P.; Abad, A.; Mattisson, T.; Lyngfelt, A. Investigation of Combined Supports for Cu-Based Oxygen Carriers for Chemical-Looping with Oxygen Uncoupling (CLOU). *Energy Fuels* **2013**, *27*, 3918–3927. [CrossRef]
18. Jiang, S.; Shen, L.; Wu, J.; Yan, J.; Song, T. The investigations of hematite-CuO oxygen carrier in chemical looping combustion. *Chem. Eng. J.* **2017**, *317*, 132–142. [CrossRef]
19. Zhao, H.; Tian, X.; Ma, J.; Su, M.; Wang, B.; Mei, D. Development of tailor-made oxygen carriers and reactors for chemical looping processes at Huazhong University of Science & Technology. *Int. J. Greenh. Gas Control.* **2020**, *93*, 102898.
20. Ismail, T.M.; Ding, L.; Ramzy, K.; Abd-El-Salam, M. Numerical and experimental analysis for simulating fuel reactor in chemical looping combustor system. *Int. J. Coal Sci. Technol.* **2020**, *7*, 551–559. [CrossRef]
21. Yang, W.; Zhao, H.; Wang, K.; Zheng, C. Synergistic effects of mixtures of iron ores and copper ores as oxygen carriers in chemical-looping combustion. *Proc. Combust. Inst.* **2015**, *35*, 2811–2818. [CrossRef]
22. Mendiara, T.; Adánez-Rubio, I.; Gayán, P.; Abad, A.; de Diego, L.F.; García-Labiano, F.; Adánez, J. Process Comparison for Biomass Combustion: In Situ Gasification-Chemical Looping Combustion (iG-CLC) versus Chemical Looping with Oxygen Uncoupling (CLOU). *Energy Technol.* **2016**, *4*, 1130–1136. [CrossRef]
23. Bao, J.; Li, Z.; Cai, N. Promoting the Reduction Reactivity of Ilmenite by Introducing Foreign Ions in Chemical Looping Combustion. *Ind. Eng. Chem. Res.* **2013**, *52*, 6119–6128. [CrossRef]
24. Siriwardane, R.; Tian, H.; Miller, D.; Richards, G. Fluidized bed testing of commercially prepared MgO-promoted hematite and $CuO\text{-}Fe_2O_3$ mixed metal oxide oxygen carriers for methane and coal chemical looping combustion. *Appl. Energy* **2015**, *157*, 348. [CrossRef]
25. Tian, X.; Zhao, H.; Ma, J. Cement bonded fine hematite and copper ore particles as oxygen carrier in chemical looping combustion. *Appl. Energy* **2017**, *204*, 242–253. [CrossRef]
26. Wang, Y.; Tian, X.; Zhao, H.; Liu, K.; Dong, Y.; Su, Z.; Zheng, C. Synergetic effects of cement bonded copper ore and red mud as oxygen carrier during in-situ gasification chemical looping combustion of coal char. *Fuel* **2021**, *303*, 121295. [CrossRef]
27. Dong, Y.; Wang, Y.; Ma, J.; Bu, H.; Zheng, C.; Zhao, H. Binary-ore oxygen carriers prepared by extrusion—Spheronization method for chemical looping combustion of coal. *Fuel Process. Technol.* **2021**, *221*, 106921. [CrossRef]
28. Zheng, T.; Li, M.; Mei, D.; Ma, J.; Wang, B.; Xu, Z. Effect of H_2S presence on chemical looping reforming (CLR) of biogas with a firebrick supported NiO oxygen carrier. *Fuel Process. Technol.* **2022**, *226*, 107088. [CrossRef]
29. World Health Organization. *S.3.6. Bulk Density and Tapped Density of Powders, Final Text for Addition to The International Pharmacopoeia*; World Health Organization: Geneva, Switzerland, 2012.
30. Ma, J.; Zhao, H.; Tian, X.; Wei, Y.; Rajendran, S.; Zhang, Y.; Bhattacharya, S.; Zheng, C. Chemical looping combustion of coal in a 5 kW_{th} interconnected fluidized bed reactor using hematite as oxygen carrier. *Appl. Energy* **2015**, *157*, 304–313. [CrossRef]

31. Cabello, A.; Gayán, P.; García-Labiano, F.; de Diego, L.F.; Abad, A.; Adánez, J. On the attrition evaluation of oxygen carriers in Chemical Looping Combustion. *Fuel Process. Technol.* **2016**, *148*, 188–197. [CrossRef]
32. Purnomo, V.; Yilmaz, D.; Leion, H.; Mattisson, T. Study of defluidization of iron-and manganese-based oxygen carriers under highly reducing conditions in a lab-scale fluidized-bed batch reactor. *Fuel Process. Technol.* **2021**, *219*, 106874. [CrossRef]
33. Mei, D.; Abad, A.; Zhao, H.; Yan, S.; Wang, B.; Yuan, Q. Extension and evaluation of a macroscopic model for syngas-fueled chemical looping combustion. *Chem. Eng. Process.* **2018**, *133*, 106–116. [CrossRef]
34. Mei, D.; Soleimanisalim, A.H.; Lyngfelt, A.; Leion, H.; Linderholm, C.; Mattisson, T. Modelling of gas conversion with an analytical reactor model for biomass chemical looping combustion (bio-CLC) of solid fuels. *Chem. Eng. J.* **2022**, *433*, 133563. [CrossRef]